POLITECNICO DI TORINO
Repository ISTITUZIONALE

Experimental evaluation of mechanical compression of lattice trusses made with Ti6Al4V for aerospace use

(Article begins on next page)

14 November 2024

Chinese Society of Aeronautics and Astronautics
& Beihang University

Chinese Journal of Aeronautics

cja@buaa.edu.cn
www.sciencedirect.com

FULL LENGTH ARTICLE

Experimental evaluation of mechanical compression of lattice trusses made with Ti6Al4V for aerospace use

Carlo Giovanni FERRO *, Sara VARETTI, Paolo MAGGIORE

Department of Mechanical and Aerospace Engineering, Politecnico di Torino, Corso Duca degli Abruzzi, Torino 10124, Italy

Abstract Lattice structures are three-dimensional structures composed of repeated geometrical shapes with multiple interconnected nodes, providing high strength-to-weight ratios, customizable properties, and efficient use of materials. A smart use of materials leads to reduced fuel consumption and lower operating costs, making them highly desirable for aircraft manufacturers. Furthermore, the customizable properties of lattice structures allow for tailoring to specific design requirements, leading to improved performance and safety for aircraft. These advantages make lattice structures an important focus for research and development in the aviation industry. This paper presents an experimental evaluation of the mechanical compression properties of lattice trusses made with Ti6Al4V, designed for use in an anti-ice system. The truss structures were manufactured using additive manufacturing techniques and tested under compressive loads to determine mechanical properties. Results showed that lattice trusses exhibited high levels of compressive strength, making them suitable for use in applications where mechanical resistance and durability are critical, such as in anti-ice systems. We also highlight the potential of additive manufacturing techniques for the fabrication of lattice trusses with tailored mechanical properties. The study provides valuable insights into the mechanical behavior of Ti6Al4V lattice trusses and their potential applications in anti-ice systems, as well as other areas where high strength-to-weight ratios are required. The results of this research contribute to the development of lightweight, efficient, and durable anti-ice systems for use in aviation and other industries.

© 2024 Production and hosting by Elsevier Ltd. on behalf of Chinese Society of Aeronautics and Astronautics. This is an open access article under the CC BY-NC-ND license (http://creativecommons.org/licenses/by-nc-nd/4.0/).

* Corresponding author.
  E-mail address: carlo.ferro@polito.it (C.G. FERRO).
Peer review under responsibility of Editorial Committee of CJA.

Production and hosting by Elsevier

1. Introduction

The aviation industry is under increasing pressure to reduce its carbon footprint due to the significant contribution it makes to global greenhouse gas emissions.[1–5] With the projected growth in air travel, the demand for more fuel-efficient and environmentally friendly aircraft is becoming a priority for manufac-

turers.[6–8] One way to achieve this goal is through the introduction of novel technologies such as Additive Manufacturing (AM).[9–11] AM offers significant benefits to the aerospace industry, including reduced material waste, increased design flexibility, and faster production times. The use of AM in aerospace products has the potential to significantly reduce the carbon footprint of aviation while also improving performance and reducing costs.[12–14] In this paper, we explore the potential of AM in aerospace products and its role in achieving a more sustainable aviation industry.

Additive manufacturing has revolutionized the manufacturing industry, providing unparalleled design freedom and the ability to create complex geometries that were previously impossible to produce.[15] One area that has seen significant interest in recent years is the use of lattice structures made with AM.[16–19] These structures, with their unique geometry and properties, have the potential to offer significant benefits in various industries, including aerospace, automotive, and medical.[20–22] Lattice structures made with AM can provide high strength-to-weight ratios, excellent energy absorption, and efficient thermal exchange properties.[23]

Traditional anti-icing systems, such as the use of hot air, have limitations in terms of weight, complexity, and effectiveness.[24–27] To address these challenges, there is a need to revolutionize anti-icing systems through the introduction of novel technologies such as trabecular structures made with additive manufacturing. Trabecular structures, with their porous, lattice-like geometry, offer a unique solution to the problem of ice accumulation on aircraft surfaces.[27–29] An artistic view of the proposed novel anti-ice system is reported in Fig. 1.[28]

Experimental compressive tests are essential in order to obtain real data and evaluate the performance of new lattice truss design.[30–33] We present an extensive analysis on different types of specimens constructed with a Design of Experiment (DOE) approach in order to identify the influence of some specifications of design on mechanical properties of the lattice structure.

The exploration of lattice structures has been a significant topic in materials science and engineering, with comprehensive studies delving into various aspects of their mechanical properties. Previous literature has extensively studied linear elasticity properties, such as stiffness in tension/compression and bending.[34–37] A key focus has also been on energy absorption and failure characteristics of lattice structures, addressing whether these exhibit quasi-brittle or elastoplastic behavior.[36,37] Moreover, the role of manufacturing inaccuracies on lattice structures, particularly geometric defects induced by Selective Laser Melting (SLM), has also been meticulously investigated.[37] Korshunova et al. extensively studied the tensile

behavior of Octet-truss lattice structures, utilizing image-based numerical characterization and experimental validation.[35] The same team also contributed to the understanding of the bending behavior of the same structures, proposing various modeling options for the same.[34] Furthermore, Al-Saedi et al. contributed valuable insights on the mechanical properties and energy absorption capability of functionally graded F2BCC lattice structures fabricated by SLM.[36] Liu et al., on the other hand, focused on the elastic and failure response of imperfect three-dimensional metallic lattices, providing critical insights into the role of geometric defects induced by SLM.[37]

The broad and intensive examination of lattice structures in the past literature provides a strong foundation for the present study. Herein, we seek to extend the current understanding by exploring the anti-ice and mechanical compression properties of Ti6Al4V lattice trusses.

The evaluation of mechanical compression of lattice trusses made with Ti6Al4V for an anti-ice system is just one part of a broader project involving several other studies and tests such as fatigue analysis[38] and CFD simulations.[39–41] Furthermore, this project involves cost evaluation studies, which aim to assess the economic feasibility of using lattice trusses made with Ti6Al4V for anti-icing systems in aircraft. The cost evaluation studies will consider factors such as material costs, production costs, and maintenance costs, providing a comprehensive analysis of the economic benefits and drawbacks of using lattice trusses in anti-icing systems.[29]

2. Materials and methods

A robust experimental design has been adopted which combines advanced materials, state-of-the-art characterization methods, and rigorous statistical analysis to systematically investigate the structure–property relationships in novel lattice structures.

Titanium alloy Ti6Al4V has been chosen for the high mechanical resistance,[42] the excellent resilience and the possibility to operate with good mechanical performance even at high temperatures.[43] This aspect permits to apply this material to anti-ice systems for fighter aircraft subjected to high thermal load in the leading edges during supersonic flight due to aerodynamic friction forces in the boundary layer.[44–46]

For the compression test specimens, a parallelepipeds sample of 20 mm × 20 mm × 40 mm has been adopted, according to previous analysis conducted.[27,29] The actual size varies from specimen to specimen according to cell dimensions in order to always maintain a discrete number of cells per side. The shape of the specimens chosen (double height compared to the side of the base) allows to analyze the fracture mechanism of the different trabecular structures that will constitute the core of the sandwich panel minimizing the border effects.

Two separate Fractional Factorial Designs (FFD) have been adopted, using the reduction of the Taguchi method.

One DOE contain only trusses-like cells while the second comprises Triply Periodical Minimal Surface (TPMS) and Auxetic cells type.

Three different parameters have been selected for each DOE: cell type, cell size and relative density. Cell type parameter affect the designed shape of the unit cell, the second parameter is the length of the cells side (all cells are cubic) and the latter parameter represents the density of the elementary cells compared to the ref-
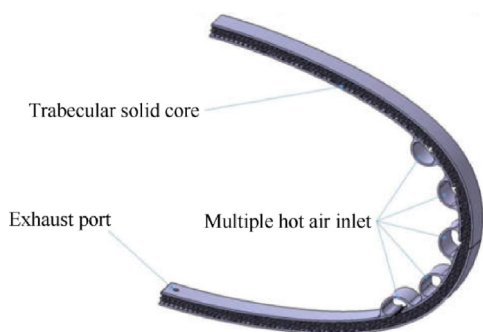

Fig. 1   Integrated anti ice panel with lattice core.[28]

erence cell bulk. Parameters and design overview are reported in Table 1 while a reference drawing is reported in Fig. 2.

Parameters for the second DOE are reported in Table 2. Photographs of all specimens manufactured are given in Appendix A.

The lattice structures evaluated were manufactured using a cutting-edge SLM 500 selective laser melting machine. SLM, an additive manufacturing technique, employs a high-power laser to fuse fine metal particles into a three-dimensional structure.[47] The process begins with the laser selectively melting a layer of powdered material, following a pattern defined by a 3D digital file. Subsequently, the powder bed is lowered, and a new layer of powder is applied. This process is repeated, layer by layer, to produce intricate and high-resolution lattice structures.[48]

Specifically, the high performance of SLM 500 machine allows for the creation of high-quality metal components, demonstrating impressive mechanical properties, geometric

Table 1   Truss cells DOE design.

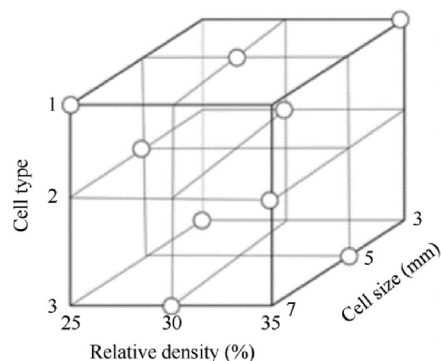| Cell type	Cell size (mm)	Relative density (%)
Bccz	3	30
	5	25
	7	35
Rhombic dodecahedron (Rhom)	3	25
	5	35
	7	30
Octet-truss (Oct)	3	35
	5	30
	7	25

Fig. 2   DOE test selection according to taguchi reduction method.

Table 2   Auxetic and TPMS cells DOE design.

Cell type	Cell size (mm)	Relative density (%)
Auxetic (Aux)	3	35
	5	30
	7	25
Gyroid (Gyr)	3	30
	5	25
	7	35
Schwartz diamond (Sch)	3	25
	5	35
	7	30

intricacy and precision, as well as a superior surface finish.[49] Its quadruple laser system guarantees high build rates and efficient production of large components.[49] We harnessed the capabilities of SLM 500 to fabricate Ti6Al4V lattice trusses with high precision, which were subsequently assessed for their mechanical compression and anti-ice properties.

All compression tests were performed with a Zwick Roell machine with a load cell of 100 kN. The tests were conducted at a constant speed of 1 mm/min and with a pre-load of 1 kN. The setup of the machine for uniaxial compression test is shown in Fig. 3.

Each specimen is presented in Section 3 labeled by a name that resumes the shape of the cell, the size of the cell and finally the relative density. For instance, the specimen Rhom-5-25-2 presents a Rhombic dodecahedron geometry, a cell size of 5 mm and a relative density of 25%. The last number in the nomenclature of specimen is the number of repetitions, in Rhom-5-25-2 case the samples is the second repetition.

The compression tests were characterized and compared using three variables obtained from stress strain curves:

- Elastic modulus (E), is obtained by the slope of the stress–strain curve in the linear elastic range.
- Maximum stress (σ_{max}), that corresponds to the peak of the curve.
- $\sigma_{0.2}$, that is the stress corresponding to a permanent plastic deformation of 0.2%.

The last value identifies the beginning of the plastic section. A line parallel to the linear elastic range and intersecting the deformation of 0.2% is drawn: $\sigma_{0.2}$ is the value at the intersection between this line and the stress strain curve. Since the dimensions of the specimens are different, values measured for the main compressive properties are also presented in Appendix B referring to the specimen density ρ, in order to compare them.

3. Results and analyses

The experimental results collected from the compressive test will be reported and discussed together with a qualitative analysis of the rupture mechanism.
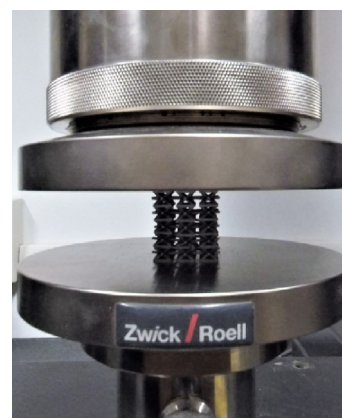

Fig. 3   Setup of Instron machine for uniaxial compression test on trabecular specimens.

3.1. Bccz specimens

Bccz specimens underwent compression tests, with the resulting stress–strain curves depicted in Fig. 4. Fig. 4 reveals that Bccz-7-35 exhibits the highest σ_{max}, accompanied by considerable plastic deformation and a 10% strain at break. Bccz-3-30, though displaying a lower σ_{max} compared to Bccz-7-35, demonstrates increased plastic deformation prior to failure and a 13% strain at break. Lastly, Bccz-5-25 possesses the lowest σ_{max} and strain at break within the group. A comprehensive list of outcomes can be found in Appendix B. Initial analysis suggests that the most influential parameter on σ_{max} value is density, with a reduction in mechanical performance from relative density of 35% to 25%, in line with the predictions of Gibson-Ashby model. Further examination of the fracture mechanism is required to better comprehend the impact of cell size.

All Bccz specimens exhibited a fracture mode characterized by buckling of the vertical struts, followed by failure of the plane at a 45° angle relative to Z-axis, consistently initiating from one of the sides of sample. Fragmentation around the damaged region subsequently transpired. Fig. 5 displays some of the tested specimens.

The stress–strain curves in Fig. 4 demonstrate a broad range of deformation preceding the failure point of the initial plane. After the collapse of the first layer, test continuation becomes infeasible due to specimen bifurcation. In the case of 3 mm cell specimens, post-first layer failure resulted in compaction of cells in proximity to the grips. This observation elucidates the stress–strain curve of the 3 mm cell specimens, characterized by an elongated and more fragmented trajectory. Consequently, the behavior of 3 mm cells aligns with that of the 5 mm and 7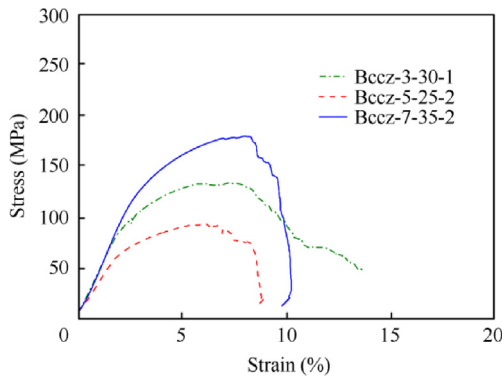 mm cells. Comparisons between stress–strain curves substantiate that an increase in relative density corresponds to enhanced mechanical outcomes.
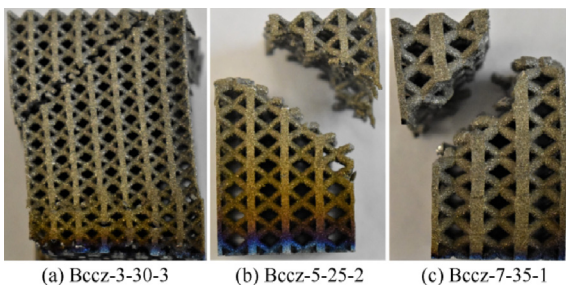
3.2. Rhombic dodecahedron specimens

Fig. 6 presents the stress–strain curves for Rhombic dodecahedron specimens. Ti6Al4V specimens with Rhombic dodecahedron cells exhibit minimal deformation before reaching the failure point across all cell sizes. Each specimen experiences failure at a strain of approximately 7%, a lower value than the 13% observed in Bccz samples. Curve comparisons confirm that increased relative density correlates with enhanced mechanical performance, albeit non-uniformly. The σ_{max} values for Rhom-7-30 and Rhom-5-35 are strikingly similar, indicating that the density disparity between these two samples does not significantly affect mechanical performance. The outcomes in terms of σ_{max}, $\sigma_{0.2}$, and E are consistent with those of Bccz and Octet-truss specimens.

For all Ti6Al4V Rhombic dodecahedron specimens, failure transpires within a limited deformation range due to strut breakage at the nodes. The failure mechanism involves the collapse of a plane at a 45° angle relative to Z-axis, initiating from a specimen corner. Subsequently, the failure of structure is accompanied by a forceful separation of specimen fragments and audible noise resulting from cell fracture. Fig. 7 depicts the tested specimens.

3.3. Octet-truss specimens

The stress–strain curves in Fig. 8 reveal that Octet-truss specimens with 5 mm and 7 mm cell sizes exhibit minimal deformation prior to the failure of the first plane. Conversely, 3 mm cell specimens display a distinct behavior, characterized by a more extensive deformation range and irregular intervals resulting from strut breakage. This divergence is attributable to the observed discrepancy between nominal and measured relative densities. This phenomenon occurs exclusively in the case of Octet-truss cells, due to their unique elementary cell structure, which impedes heat diffusion during the production process and consequently leads to the adhesion of un-melted powders. While the model assumes a relative density of 35%, the experimentally measured value for 3 mm cells is 51%.[50] Comparisons among the stress–strain curves corroborate that increased relative density is associated with improved mechan-

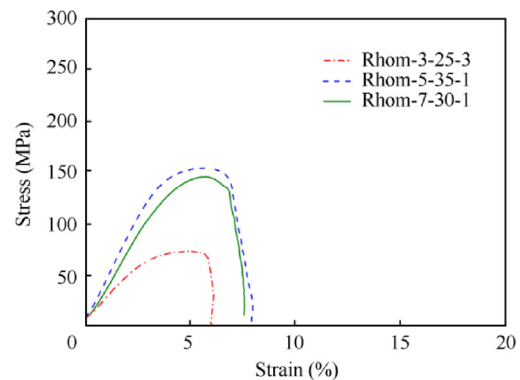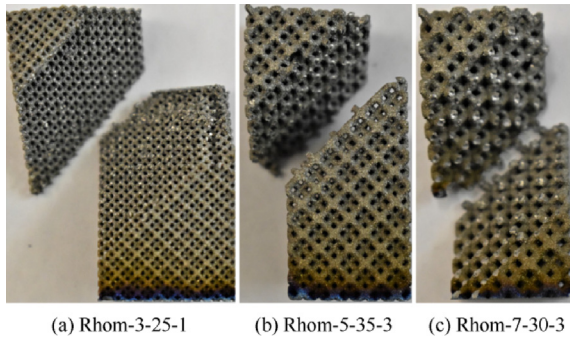**Fig. 4**   Stress–strain curves for Ti6Al4V Bccz specimens.

(a) Bccz-3-30-3   (b) Bccz-5-25-2   (c) Bccz-7-35-1

Fig. 5   Tested Bccz specimens.

Fig. 6   Stress–strain curves for Ti6Al4V Rhombic dodecahedron specimens.

(a) Rhom-3-25-1   (b) Rhom-5-35-3   (c) Rhom-7-30-3

Fig. 7 Tested Rhombic dodecahedron specimens.

Fig. 8 Stress–strain curves for Ti6Al4V Octet-truss specimens.

(a) Oct-3-35-1   (b) Oct-5-30-2   (c) Oct-7-25-3
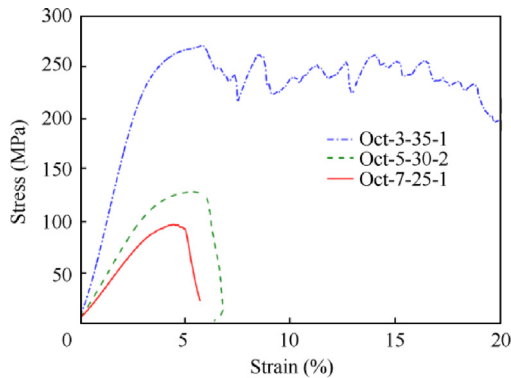
Fig. 9 Tested Octet-truss specimens.
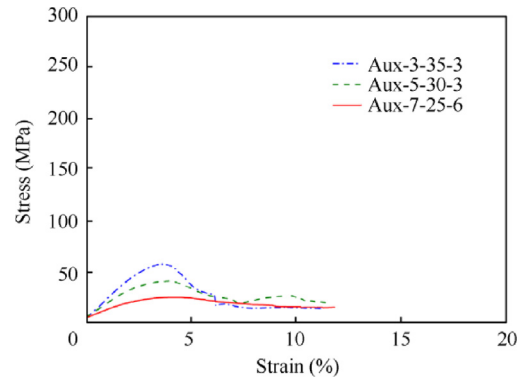
Fig. 10 Stress–strain curves for Ti6Al4V Auxetic specimens.

ical outcomes, in alignment with the prediction of Gibson-Ashby model.

In all Ti6Al4V Octet-truss specimens, failure is observed within a limited deformation range as a result of strut fractures at the nodes. The failure initiates from a specimen corner and propagates along a plane oriented at a 45° angle with respect to Z-axis. This structural collapse is accompanied by a forceful disintegration of specimen segments and the audible noise produced by the fracturing of individual cells. Notably, for Octet-truss cells alone, the 3 mm cell exhibits atypical behavior, characterized by a densification phase and the concurrent failure of multiple planes. Representative specimens are depicted in Fig. 9.

3.4. Auxetic specimens

Fig. 10 presents the stress–strain curves for Auxetic specimens, which display irregular regions corresponding to strut fractures. The mechanical outcomes, including maximum stress (σ_{max}), yield stress ($\sigma_{0.2}$), and elastic modulus (E), are lower in comparison to those of other cell geometries.

Ideally, Auxetic structures should exhibit compaction during uniaxial compression testing and provide enhanced resistance due to a negative Poisson's coefficient. While some tested Auxetic cells display this behavior, compacting and increasing the density of the resistance section as the fracture initiates from the cell nodes, the overall mechanical performance remains unsatisfactory if compared to other cells. Moreover, several specimens experience failure due to horizontal strut fractures, leading to the separation of specimen into
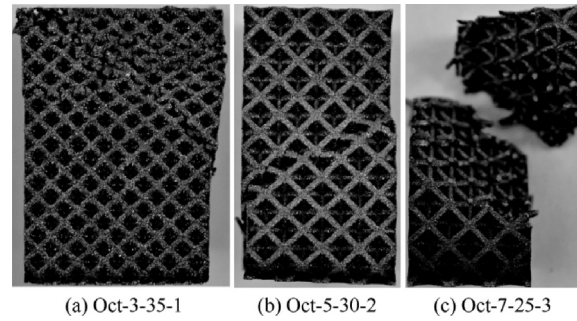
layers. Additionally, as illustrated in Figs. 11(a) and (b), some samples undergo lateral cell collapse, causing a rippling effect throughout the specimen. This effect is caused by local imperfection in the beams of cells. Further optimization of the original model is necessary for the effective application of these cells.

3.5. Gyroid specimens

Fig. 12 displays the stress–strain curves for Gyroid specimens, which demonstrate superior mechanical performance compared to previous specimen types in terms of maximum stress (σ_{max}), yield stress ($\sigma_{0.2}$), and elastic modulus (E), as summarized in Appendix B. A comparison of the curves reveals that an increase in relative density corresponds to enhanced mechanical performance. All specimens exhibit significant plastic deformation prior to failure, which consistently occurs at approximately 12% strain.

The Gyroid models, generated through the manipulation of three-dimensional surfaces, lack struts unlike other geometries.

(a) Aux-3-35-1   (b) Aux-5-30-2   (c) Aux-7-25-5

Fig. 11 Tested Auxetic specimens.

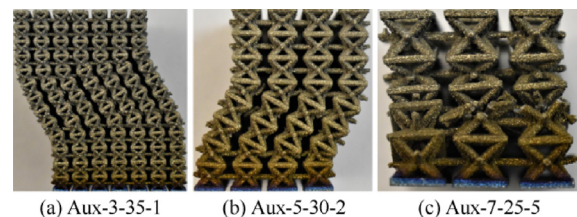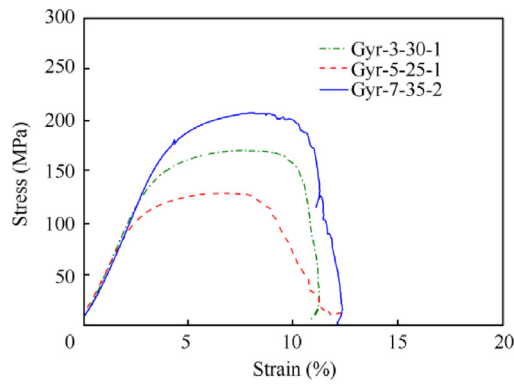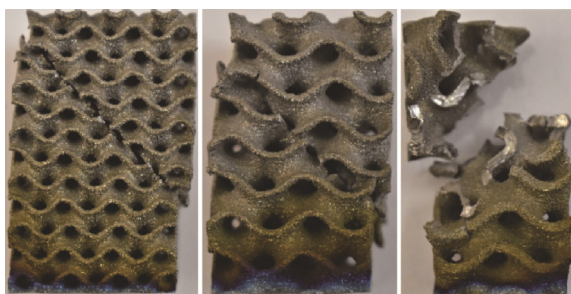**Fig. 12** Stress–strain curves for Ti6Al4V Gyroid specimens.

Fig. 14 Stress–strain curves for Ti6Al4V Schwartz diamond specimens.

Similar to the Bccz specimens, all Gyroid specimens fracture by collapsing along a plane oriented at a 45° angle with respect to Z-axis, initiating from one side of the specimen. The fracture progresses with the disintegration of specimen and the subsequent collapse of the cells. For the 5 mm and 7 mm specimens, the fracture may propagate more irregularly, following the contours of the three-dimensional surface. The tested specimens are illustrated in Fig. 13.

3.6. Schwartz diamond specimens

Fig. 14 displays the stress–strain curves for Schwartz diamond specimens, which exhibit marginally enhanced mechanical properties—including maximum stress (σ_{max}), yield stress ($\sigma_{0.2}$), and elastic modulus (E)—compared to Gyroid cells. The behavior showcased in the curves closely resembles that of Gyroid specimens, characterized by plastic deformation prior to failure. However, in this case, fractures occur at a lower strain (approximately 10%) for all specimens. As the comparison of the curves suggests an increase in relative density results in improved mechanical performance.

Similar to Gyroid models, Schwartz diamond models are generated through the manipulation of three-dimensional surfaces and lack struts, unlike other geometries. All Schwartz diamond specimens fracture by collapsing along a plane oriented at a 45° angle with respect to Z-axis, initiating from one side of the specimen, as observed in the Bccz specimens. The fracture progresses with the disintegration of the specimen and the subsequent collapse of the cells. For the 5 mm and 7 mm specimens, the fracture may propagate more irregularly,

following the contours of the three-dimensional surface. The tested specimens are depicted in Fig. 15.

4. Discussion

The data collected in Section 3 will be discussed and compared in order to evaluate new insights on the influence of design parameters.

4.1. DOE analysis

Observing the data interval plot from Fig. 16, it is possible to evidence some non-uniformities between the amplitude of the distributions of experimental outcomes. The observed discrepancies in certain results may stem from the fact that, as substantiated by both simulations and experimental findings, a limited number of cells (3, 5, 7) can induce what is referred to as size effects in various deformation modes, even within the elastic range, with bending in triangular and octet lattices serving as illustrative examples.[34]

Generally, for both elastic modulus evaluation and for σ_{max} the variability among trusses structure is greater than the one observed by TPMS or Auxetic. A possible explanation of those phenomena may lie in the fact that beam foams have geometries much more intricate and so more sensible to the manufacturing imperfections. Manufacturing technique, in other terms, insert small variability that are amplified by the cell design. The only exception is represented by $\sigma_{0.2}$ where for Auxetic

Fig. 13 Tested Gyroid specimens.
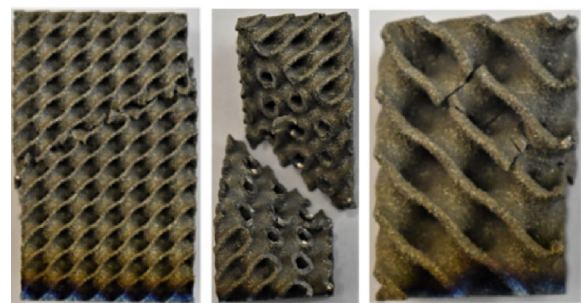
Fig. 15 Tested Schwartz diamond specimens.
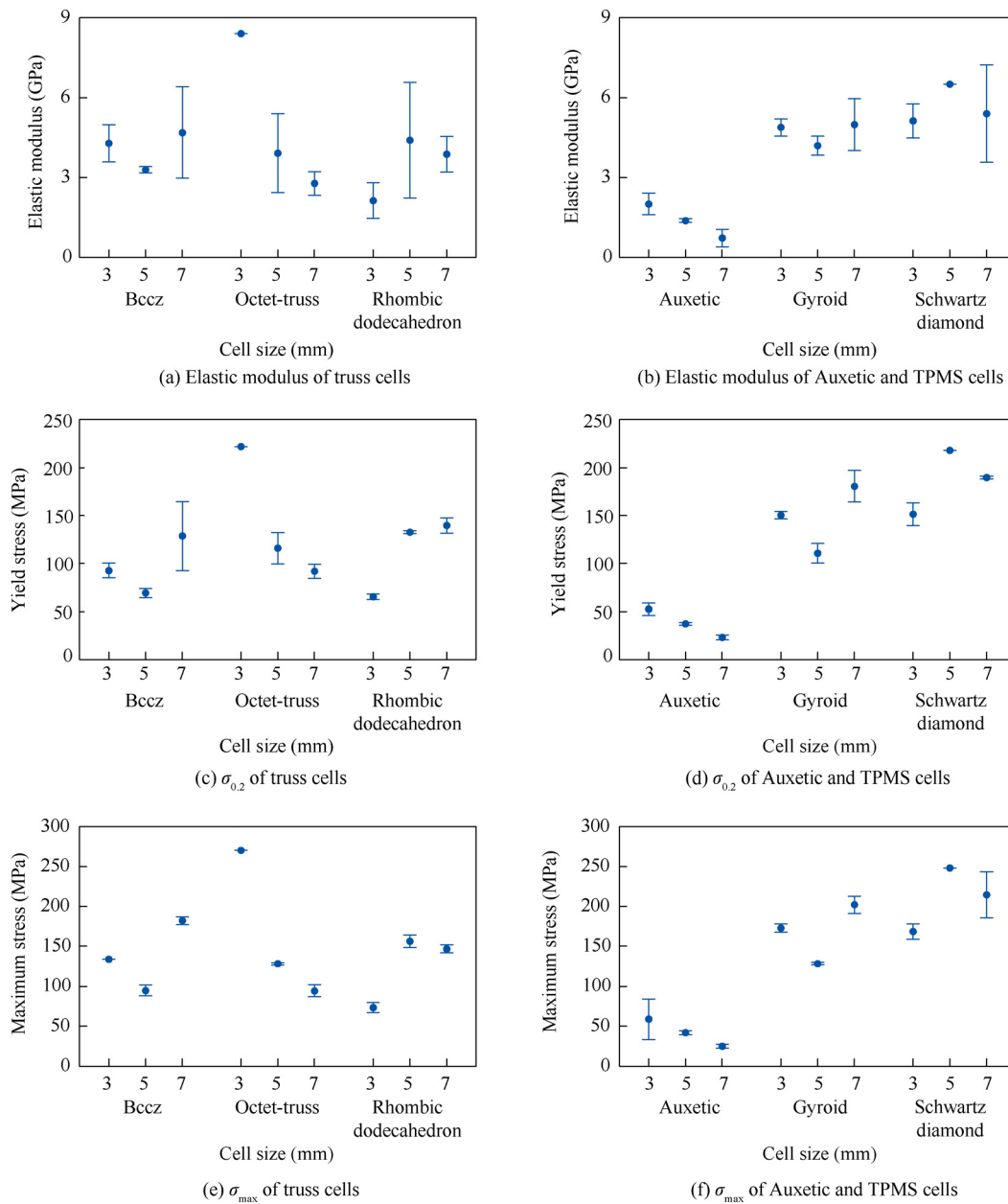
Fig. 16   Interval plots of DOE.

with 3 mm cells and Schwartz diamond with 7 mm cells. These two cases may be outliers with special defects occurred during the manufacturing or in the tests. Further investigations are needed.

The second evaluation extrapolated from the DOE is reported in Fig. 17 and is represented by the main effect.

Figs. 17(a) and (b) show the effect of the three factors (cell type, cell size, and relative density) on elastic modulus. The evidence suggests that cell type is the primary determinant of elastic modulus. The highest elasticity coefficient for truss cells was obtained by Octet-truss for truss cells, and by Schwartz diamond for TPMS structures. Relative density shows a positive linear trend with the increase of relative density in all cases. Regarding cell size, the truss cell exhibits a decreasing trend with increasing cell size, plateauing after 5 mm. In contrast, Auxetic and TPMS cells show an opposite curvature, only decrease after 5 mm.

For the yield stress $\sigma_{0.2}$ and for the maximum stress σ_{max} the evaluations are quite similar. Relative density plays always a beneficial role with a behavior almost linear in all the evaluated outcome.

Cell size is the less important factor with a slightly beneficial impact on TPMS and Auxetic and instead with a positive quadratic trend for trusses cells with a minimum in correspondence of 5 mm case.

Cell type instead maintain stable and coherent outcome with the evaluation for elastic modulus. The best cell for the truss structure is always represented by Octet-truss and the best for TPMS is represented as before by Schwartz diamond cells.
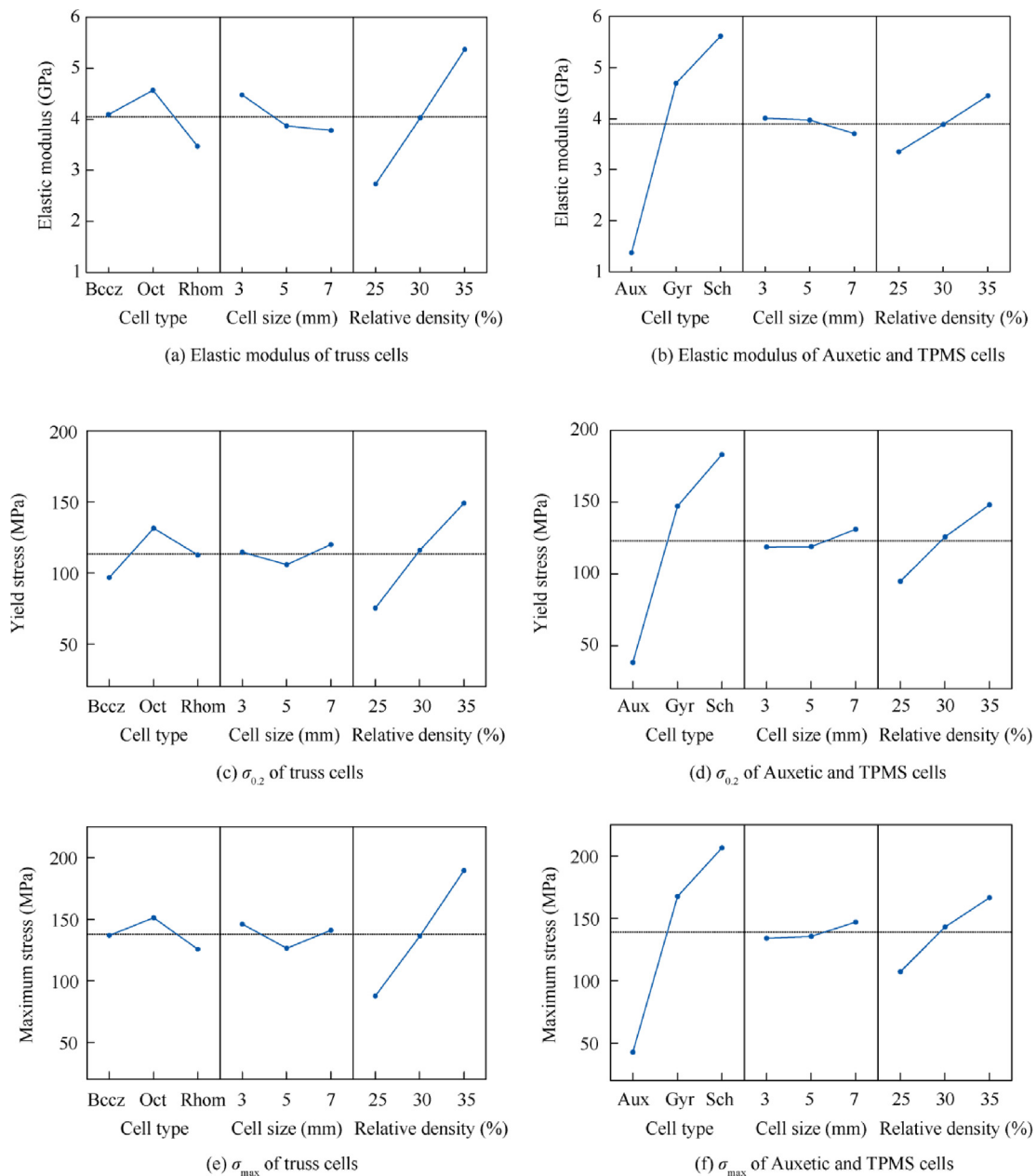
Fig. 17   Main effect plot of DOE.

4.2. Comparison with Gibson-Ashby model

The experimental data obtained for all six cell geometries is compared with the Gibson-Ashby model for open-cell foams. The Gibson-Ashby model expresses the mechanical properties of the foam as relative values concerning an equivalent solid with identical dimensions and material composition. The relative density, compressive modulus, and compressive strength are calculated using

$$\rho_r = \rho_f/\rho_s \tag{1}$$

$$E_f/E_s = C_1(\rho_f/\rho_s)^2 \tag{2}$$

$$\sigma_f/\sigma_s = C_2(\rho_f/\rho_s)^{1.5} \tag{3}$$

where ρ_f and ρ_s are the densities of the foam and solid, respectively; E_f and E_s are the elastic moduli of the foam and solid, respectively; σ_f and σ_s are the compressive strengths of the foam and solid, respectively; C_1 and C_2 are Gibson-Ashby constants. Constants C_1 and C_2 encapsulate all geometric proportionality features and are detailed in Appendix C.

The model enables the determination of maximum strengths and elastic modulus for trabecular specimens using the density and mechanical properties of the foam and corresponding dense material. The mechanical properties of fully dense Ti6Al4V alloy components were sourced from the EOS datasheet,[51] indicating a compressive σ_{max} = 1215 MPa, E = 110 GPa, and ρ_s = 4.41 kg/dm³. Fig. 18 reports a comparison between experimental data for Bccz, Octet-truss and Rhombic dodecahedron cells in Ti6Al4V with the values
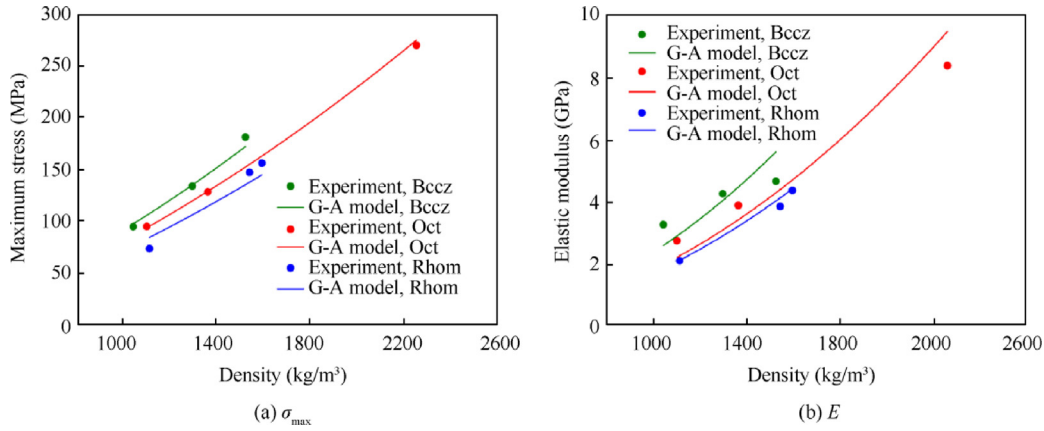
Fig. 18   Comparison between experimental data for Bccz, Octet-truss and Rhombic dodecahedron cells in Ti6Al4V with values obtained from Gibson-Ashby model for the same cells in terms of σ_{max} and E.

Fig. 19   Comparison between experimental data for Auxetic, Gyroid and Schwartz diamond cells in Ti6Al4V with values obtained from Gibson-Ashby model for the same cells in terms of σ_{max} and E.

obtained from Gibson-Ashby (G-A) model for the same cells in terms of (A) σ_{max} and (B) Elastic modulus. Fig. 18(a) displays σ_{max} results. The model and experimen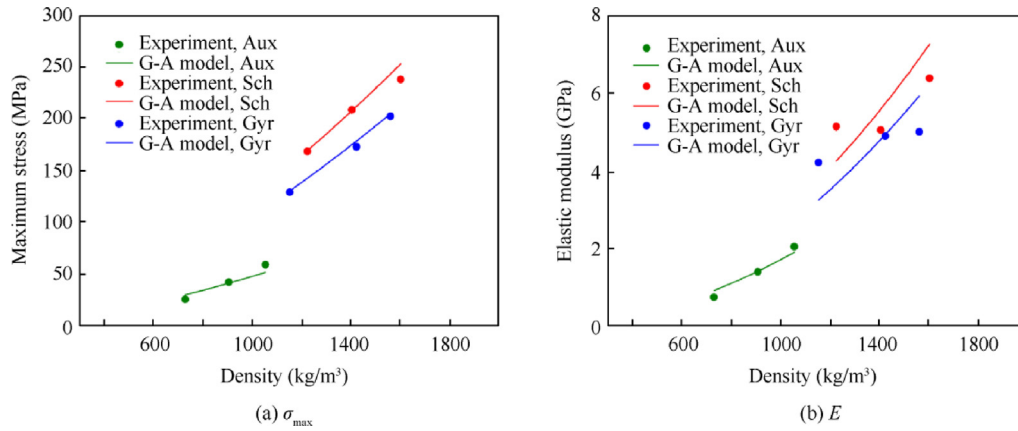tal data align well across all densities, as Ti6Al4V experiences minimal density increase in 3 mm cells, as reported by Ref. 27. Fig. 18(b) presents the elastic modulus results. Elastic modulus correspondence between experimental data and the model is weaker, revealing how trabecular structure fracture behaviors differ from those of the foam. The divergence between the model and experimental data is particularly pronounced for Bccz cells, while Octet-truss and Rhombic dodecahedron cells exhibit a less marked discrepancy, as their fracture mechanisms more closely resemble foam behavior with brittle cell collapse.

Fig. 19 compares the experimental data and Gibson-Ashby model predictions for the second set of specimens subjected to uniaxial compression tests, including Auxetic, Gyroid, and Schwartz diamond geometries. Fig. 19(a) shows σ_{max} results. The model aligns well with the experimental data for all cell geometries. In contrast, Fig. 19(b) illustrates the opposite scenario: the model struggles to predict the elastic modulus, particularly for Gyroid and Schwartz diamond cells, due to their three-dimensional surface designs and significant deviation from foam behavior. The theoretical and experimental elastic

modulus for Auxetic cells exhibit similar trends, as their fracture and densification characteristics resemble foam structures.

5. Conclusions

In conclusion, this study has successfully demonstrated the potential of Ti6Al4V lattice trusses in anti-ice systems, particularly when manufactured using additive manufacturing techniques. The experimental evaluation revealed high compressive strength in the lattice trusses, making them suitable for applications requiring mechanical resistance and durability. Furthermore, the customizable properties of lattice structures allow for improved performance and safety in aircraft design.

The discussion of the results highlights the influence of design parameters on the mechanical properties of lattice trusses. The variability observed among truss structures was greater than that of TPMS or Auxetic structures, which could be attributed to the intricate geometries of beam foams being less tolerant to imperfections introduced during manufacturing. Additionally, the comparison with the Gibson-Ashby model showed good alignment for σ_{max} across all densities, while the correspondence for elastic modulus was weaker, sug-

gesting that trabecular structure fracture behaviors differ from those of foam.

The results obtained from our study align well with previous investigations in the field, such as the work carried out by Xiao et al., where they explored the compressive performance and energy absorption of additively manufactured metallic hybrid lattice structures.[52] The failure mechanism reported in their work was also observed in the tests conducted in our laboratory, further affirming the validity of their findings. Moreover, our research contributes new insights to the field, particularly through the use of a Design of Experiments (DOE) approach. This method allowed us to delve into the impact of cell design parameters on structural performance, broadening the current understanding of these complex systems.

The insights gained from this research contribute to the ongoing development of lightweight, efficient, and durable anti-ice systems for use in aviation and other industries. The adoption of lattice structures in aircraft design, along with the advancements in additive manufacturing techniques, can significantly reduce fuel consumption and lower operating costs, leading to more environmentally friendly and cost-effective transportation. Future work should focus on further investigation of the observed variability in mechanical properties and refining manufacturing processes to enhance the performance of lattice trusses in anti-ice systems and other applications requiring high strength-to-weight ratios.

Declaration of competing interest

The authors declare that they have no known competing financial interests or personal relationships that could have appeared to influence the work reported in this paper.

Appendix A. Photographs of manufactured specimens

(a) Bccz, cell size is 3 mm, relative density is 30%

(b) Rhom, cell size is 3 mm, relative density is 25%

(c) Oct, cell size is 3 mm, relative density is 35%

(d) Aux, cell size is 3 mm, relative density is 35%

(e) Gyr, cell size is 3 mm, relative density is 30%

(f) Sch, cell size is 3 mm, relative density is 25%

(g) Bccz, cell size is 5 mm, relative density is 25%

(h) Rho, cell size is 5 mm, relative density is 35%

(i) Oct, cell size is 5 mm, relative density is 30%

(j) Aux, cell size is 5 mm, relative density is 30%

(k) Gyr, cell size is 5 mm, relative density is 25%

(l) Sch, cell size is 5 mm, relative density is 35%

(m) Bccz, cell size is 7 mm, relative density is 35%

(n) Rhom, cell size is 7 mm, relative density is 30%

(o) Oct, cell size is 7 mm, relative density is 25%

(p) Aux, cell size is 7 mm, relative density is 25%

(q) Gyr, cell size is 7 mm, relative density is 35%
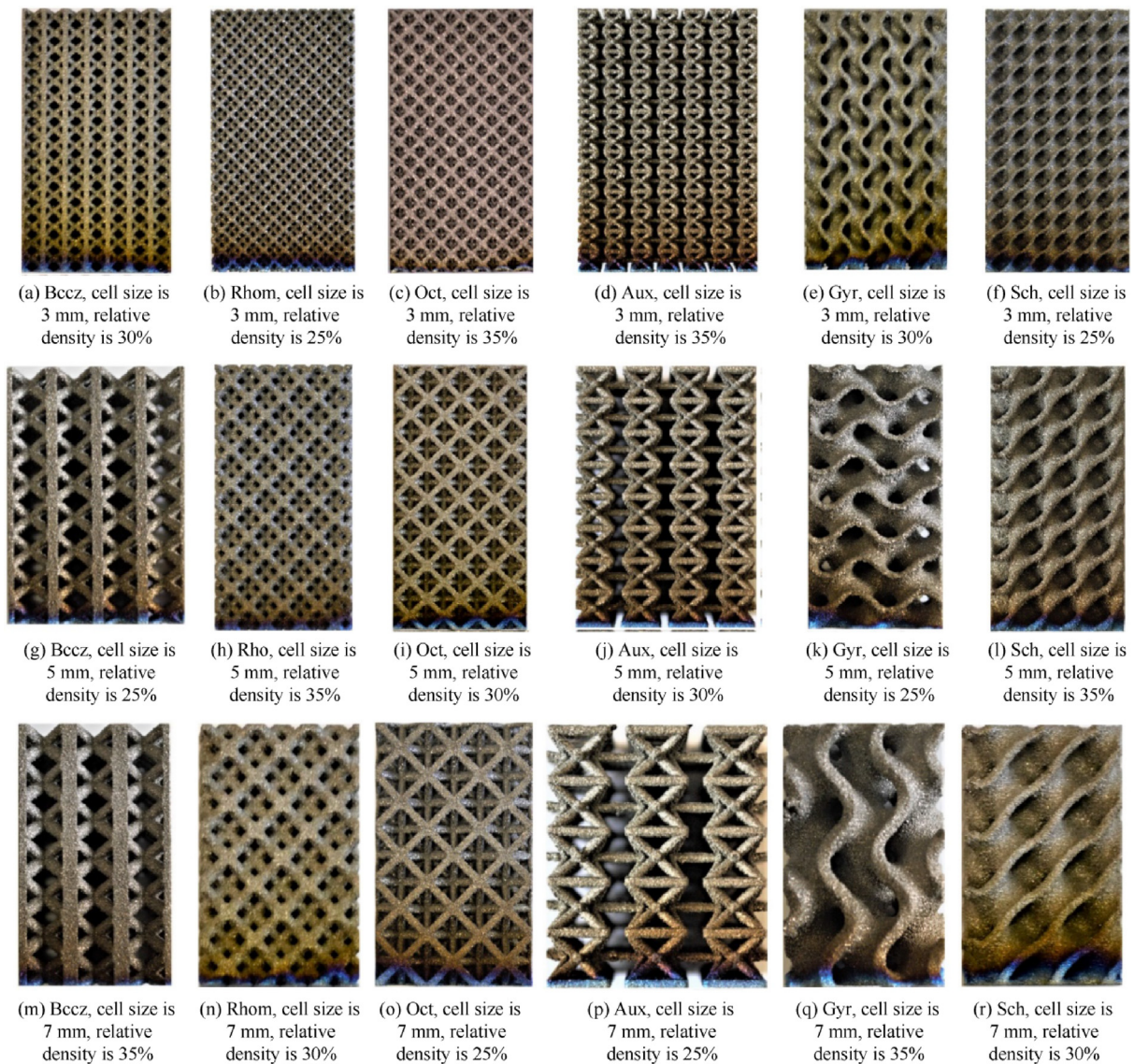
(r) Sch, cell size is 7 mm, relative density is 30%

Fig. A1 Photographs of manufactured specimens.

Appendix B. Experimental collected results

Table B1 Experimental results of compression tests.

Specimen type	σ_{max} (MPa)	$\sigma_{0.2}$ (MPa)	E (MPa)	σ_{max}/ρ (MPa·m³/kg)	$\sigma_{0.2}/\rho$ (MPa·m³/kg)	E/ρ (MPa·m³/kg)
Bccz-3-30-1	134	96	4344	0.103	0.0733	3.33
Bccz-3-30-2	134	90	3983	0.102	0.0685	3.04
Bccz-3-30-3	134	92	4544	0.105	0.0726	3.58
Bccz-5-25-1	98	71	3349	0.0931	0.0677	3.18
Bccz-5-25-2	94	69	3251	0.0892	0.0657	3.10
Bccz-5-25-3	93	67	3295	0.0909	0.0660	3.23
Bccz-7-35-1	184	112	3931	0.119	0.0725	2.54
Bccz-7-35-2	180	138	4848	0.112	0.0918	3.23
Bccz-7-35-3	182	136	5288	0.120	0.0895	3.48
Rhom-3-25-1	71	64	1827	0.0659	0.0589	1.68
Rhom-3-25-2	76	66	2304	0.0663	0.0583	2.02
Rhom-3-25-3	74	66	2279	0.0665	0.0594	2.06
Rhom-5-35-1	154	133	4221	0.0987	0.0853	2.71
Rhom-5-35-2	155	132	3630	0.0987	0.0837	2.31
Rhom-5-35-3	160	133	5349	0.0972	0.0809	3.25
Rhom-7-30-1	145	136	3713	0.0959	0.0894	2.45
Rhom-7-30-2	147	141	3746	0.0954	0.0912	2.43
Rhom-7-30-3	149	142	4193	0.0956	0.0909	2.68
Oct-3-35-1	270	222	8402	0.119	0.0976	3.69
Oct-3-35-2						
Oct-3-35-3						
Oct-5-30-1	128	110	3637	0.0947	0.0809	2.68
Oct-5-30-2	129	115	3512	0.0951	0.0844	2.58
Oct-5-30-3	128	123	4602	0.0933	0.0897	3.36
Oct-7-25-1	98	95	2716	0.0872	0.0848	2.42
Oct-7-25-2	94	92	2643	0.0871	0.0848	2.44
Oct-7-25-3	92	89	2984	0.0847	0.0813	2.73
Aux-3-35-2	61	52	2041	0.0569	0.0482	1.91
Aux-3-35-3	57	53	1977	0.0541	0.0497	1.87
Aux-5-30-1	43	38	1370	0.0468	0.0411	1.50
Aux-5-30-2	42	37	1365	0.0456	0.0408	1.49
Aux-5-30-3	41	37	1417	0.0455	0.0418	1.59
Aux-7-25-1						
Aux-7-25-2						
Aux-7-25-3						
Aux-7-25-4	24	22	574	0.0324	0.0297	0.77
Aux-7-25-5	26	24	788	0.0355	0.0316	1.06
Aux-7-25-6	25	23	822	0.0329	0.0309	1.10
Gyr-3-30-1	171	149	4743	0.122	0.105	3.37
Gyr-3-30-2	175	152	4916	0.122	0.106	3.44
Gyr-3-30-3	172	150	4996	0.120	0.105	3.49
Gyr-5-25-1	129	106	4082	0.111	0.0909	3.51
Gyr-5-25-2	128	112	4361	0.114	0.0991	3.87
Gyr-5-25-3	129	114	4155	0.110	0.0975	3.55
Gyr-7-35-1	200	179	4730	0.129	0.115	3.04
Gyr-7-35-2	207	188	4809	0.131	0.118	3.04
Gyr-7-35-3	199	175	5441	0.129	0.113	3.53
Sch-3-25-1	170	155	5122	0.138	0.125	4.14
Sch-3-25-2	171	153	4877	0.139	0.125	3.97
Sch-3-25-3	164	146	5388	0.135	0.121	4.46
Sch-5-35-1						
Sch-5-35-2	248	218	6495	0.154	0.135	4.03
Sch-5-35-3						
Sch-5-35-4	228	189	6246	0.143	0.118	3.91
Sch-7-30-1	208	190	4935	0.148	0.136	3.53
Sch-7-30-2	208	190	5013	0.151	0.138	3.65

Appendix C. Gibson-Ashby constants

Table C1 C_1 and C_2 **constants for Gibson-Ashby model calculations**.

Specimen type	C_1	C_2
Bccz-3-30	0.70	0.43
Bccz-5-25	0.70	0.43
Bccz-7-35	0.70	0.43
Rhom-3-25	0.55	0.31
Rhom-5-35	0.55	0.31
Rhom-7-30	0.55	0.31
Oct-3-35	0.62	0.33
Oct-5-30	0.62	0.33
Oct-7-25	0.62	0.33
Aux-3-35	0.36	0.30
Aux-5-30	0.36	0.30
Aux-7-25	0.36	0.30
Gyr-3-30	0.80	0.43
Gyr-5-25	0.80	0.43
Gyr-7-35	0.80	0.43
Sch-3-25	0.95	0.50
Sch-5-35	0.95	0.50
Sch-7-30	0.95	0.50

References

1. Fahey DW, Lee DS. Aviation and the impacts of climate change: A scientific perspective. *Carbon Clim Law Rev* 2016;**10**(2):97–104.
2. Klöwer M, Allen MR, Lee DS, et al. Quantifying aviation's contribution to global warming. *Environ Res Lett* 2021;**16**(10):104027.
3. Whitmarsh L, Capstick S, Moore I, et al. Use of aviation by climate change researchers: Structural influences, personal attitudes, and information provision. *Glob Environ Change* 2020;**65**:102184.
4. Lee DS, Fahey DW, Forster PM, et al. Aviation and global climate change in the 21st century. *Atmos Environ* 2009;**43**(22–23):3520–37.
5. Baxter G. Assessing the carbon footprint and carbon mitigation measures of a major full-service network airline: A case study of Singapore airlines. *Int J Environ Agric Biotechnol* 2022;**7**(5):81–107.
6. Afonso F, Sohst M, Diogo CMA, et al. Strategies towards a more sustainable aviation: A systematic review. *Prog Aerosp Sci* 2023;**137**:100878.
7. Zakharenko R, Luttmann A. Downsizing the jet: A forecast of economic effects of increased automation in aviation. *Transp Res Part B Methodol* 2023;**170**:25–47.
8. Wu X, Blake A. The impact of the COVID-19 crisis on air travel demand: Some evidence from China. *SAGE Open* 2023;**13**(1):215824402311524.
9. Abrantes I, Ferreira AF, Silva A, et al. Sustainable aviation fuels and imminent technologies—CO_2 emissions evolution towards 2050. *J Clean Prod* 2021;**313**:127937.
10. Zaporozhets O, Isaienko V, Synylo K. Trends on current and forecasted aircraft hybrid electric architectures and their impact on environment. *Energy* 2020;**211**:118814.
11. Lai YY, Christley E, Kulanovic A, et al. Analysing the opportunities and challenges for mitigating the climate impact of aviation: A narrative review. *Renew Sustain Energy Rev* 2022;**156**:111972.
12. Qin RY, Zhang GD, Li N, et al. Research progress on additive manufacturing of TiAl-based alloys. *J Mech Eng* 2021;**57**(8):115–32 [Chinese].
13. Zhang X, Liang EQ. Metal additive manufacturing in aircraft: Current application, opportunities and challenges. *IOP Conf Ser: Mater Sci Eng* 2019;**493**:012032.
14. Blakey-Milner B, Gradl P, Snedden G, et al. Metal additive manufacturing in aerospace: a review. *Mater Des* 2021;**209**:110008.
15. Bhavar V, Kattire P, Patil V, et al. A review on powder bed fusion technology of metal additive manufacturing. *Additive manufacturing handbook: Product development for the defense industry*. New York: CRC Press; 2017. p. 251–61.
16. Benedetti M, du Plessis A, Ritchie RO, et al. Architected cellular materials: A review on their mechanical properties towards fatigue-tolerant design and fabrication. *Mater Sci Eng R Rep* 2021;**144**:100606.
17. Burns N. Why AM now has the potential to revolutionise filtration solutions. *Filtr + Sep* 2014;**51**(2):42–3.
18. du Plessis A, Razavi N, Benedetti M, et al. Properties and applications of additively manufactured metallic cellular materials: a review. *Prog Mater Sci* 2022;**125**:100918.
19. Korkmaz ME, Gupta MK, Robak G, et al. Development of lattice structure with selective laser melting process: A state of the art on properties, future trends and challenges. *J Manuf Process* 2022;**81**:1040–63.
20. Chen LY, Liang SX, Liu YJ, et al. Additive manufacturing of metallic lattice structures: Unconstrained design, accurate fabrication, fascinated performances, and challenges. *Mater Sci Eng R Rep* 2021;**146**:100648.
21. Beyer C, Figueroa D. Design and analysis of lattice structures for additive manufacturing. *J Manuf Sci Eng* 2016;**138**(12):121014.
22. Dong GY, Tang YL, Zhao YF. A survey of modeling of lattice structures fabricated by additive manufacturing. *J Mech Des* 2017;**139**(10):100906.
23. H. Gharehbaghi, A. Farrokhabadi and Z. Noroozi, Introducing a new hybrid surface strut-based lattice structure with enhanced energy absorption capacity, *Mech Adv Mater Struct* [Internet]. 2023 Jan 18. Available from: https://doi.org/10.1080/15376494.2023.2167246.
24. Thomas SK, Cassoni RP, MacArthur CD. Aircraft anti-icing and de-icing techniques and modeling. *J Aircr* 1996;**33**(5):841–54.
25. Tenebre P, Six MF. Anti-icing/de-icing system and method and aircraft structure incorporating this system. United States patent: US8146866B2. 2009 Mar 5.
26. Mclaren D. Thermal anti-icing system for aircraft. United States patent: 5011098. 1991.
27. Ferro CG, Varetti S, Maggiore P, et al. Design and characterization of trabecular structures for an anti-icing sandwich panel produced by additive manufacturing. *J Sandw Struct Mater* 2020;**22**(4):1111–31.
28. Ferro CG, Varetti S, Vitti F. Thermal anti ice system integrated in the structure and method for its fabrication. Italy patent: IT102016000098196A1. 2016.
29. Ferro C, Varetti S, Vitti F, et al. A robust multifunctional sandwich panel design with trabecular structures by the use of additive manufacturing technology for a new de-icing system. *Technologies* 2017;**5**(2):35.
30. Emir E, Bahçe E, Uysal A. Effect of octet-truss lattice transition geometries on mechanical properties. *J Mater Eng Perform* 2021;**30**(12):9370–6.
31. Sienkiewicz J, Płatek P, Jiang FC, et al. Investigations on the mechanical response of gradient lattice structures manufactured via SLM. *Metals* 2020;**10**(2):213.
32. Riva L, Ginestra PS, Ceretti E. Mechanical characterization and properties of laser-based powder bed–fused lattice structures: A review. *Int J Adv Manuf Technol* 2021;**113**(3):649–71.

33. Mantovani S, Giacalone M, Merulla A, et al. Effective mechanical properties of AlSi7Mg additively manufactured cubic lattice structures. *3D Print Addit Manuf* 2022;**9**(4):326–36.

34. Korshunova N, Alaimo G, Hosseini SB, et al. Bending behavior of octet-truss lattice structures: Modelling options, numerical characterization and experimental validation. *Mater Des* 2021;**205**:109693.

35. Korshunova N, Alaimo G, Hosseini SB, et al. Image-based numerical characterization and experimental validation of tensile behavior of octet-truss lattice structures. *Addit Manuf* 2021;**41**:101949.

36. Al-Saedi DSJ, Masood SH, Faizan-Ur-Rab M, et al. Mechanical properties and energy absorption capability of functionally graded F2BCC lattice fabricated by SLM. *Mater Des* 2018;**144**:32–44.

37. Liu L, Kamm P, García-Moreno F, et al. Elastic and failure response of imperfect three-dimensional metallic lattices: The role of geometric defects induced by selective laser melting. *J Mech Phys Solids* 2017;**107**:160–84.

38. Ferro CG, Varetti S, Maggiore P. Experimental evaluation of fatigue strength of AlSi10Mg lattice structures fabricated by AM. *Aerosp* 2023;**10**(5):400.

39. Perello M, Ferro CG. *Numerical simulation and experimental validation of lattice structures for an innovative anti-ice leading edge*. Torino: Politecnico di Torino; 2018.

40. Champvillair D. *Numerical and experimental validation of an innovative anti ice panel by means of computational fluid dynamics*. Torino: Politecnico di Torino; 2018.

41. Ferro CG, Maggiore P, Champvillair D. Development of a computational fluid dynamics model for ice formation: Validation and parameter analysis. *Atmos* 2023;**14**(5):834.

42. Bartolomeu F, Gasik M, Silva FS, et al. Mechanical properties of Ti6Al4V fabricated by laser powder bed fusion: A review focused on the processing and microstructural parameters influence on the final properties. *Metals* 2022;**12**(6):986.

43. Wu BT, Pan ZX, Ding DH, et al. Effects of heat accumulation on microstructure and mechanical properties of Ti6Al4V alloy deposited by wire arc additive manufacturing. *Addit Manuf* 2018;**23**:151–60.

44. Tsvetkov OI, Reznik SV, Samsonov KS. Thermocontrol for a space tourism vehicle model. *AIP Conf Proc* 2021;**2318**(1):020013.

45. Mao YF, Li YZ, Wang JX, et al. Cooling ability/capacity and exergy penalty analysis of each heat sink of modern supersonic aircraft. *Entropy* 2019;**21**(3):223.

46. Lee HB, Kim YN, Choi IJ, et al. Nonlinear dynamic responses of shear-deformable composite panels under combined supersonic aerodynamic, thermal, and random acoustic loads. *Int J Aeronaut Space Sci* 2020;**21**(3):707–22.

47. Fayazfar H, Salarian M, Rogalsky A, et al. A critical review of powder-based additive manufacturing of ferrous alloys: Process parameters, microstructure and mechanical properties. *Mater Des* 2018;**144**:98–128.

48. Thijs L, Verhaeghe F, Craeghs T, et al. A study of the microstructural evolution during selective laser melting of Ti–6Al–4V. *Acta Mater* 2010;**58**(9):3303–12.

49. SLM Solutions Group AG. SLM®500: The high power machine for metal additive manufacturing [Internet]. 2023. Available from: https://www.slm-solutions.com/en/products-and-solutions/machines/slm-500/.

50. Varetti S. Study and development of an innovative L-PBF demonstrator and an anti-ice solution based on trabecular structures. Torino: Politecnico di Torino; 2020.

51. EOS GmbH – Electro Optical Systems. EOS titanium Ti64 grade 5 material data sheet; 2023.

52. Xiao LJ, Xu X, Feng GZ, et al. Compressive performance and energy absorption of additively manufactured metallic hybrid lattice structures. *Int J Mech Sci* 2022;**219**:107093.